

**Final Technical Report on**  
**NASA-Langley Award # NAG-1-1925**  
*Swept-Wing Receptivity Studies Using Distributed Roughness*

**1 June 1997 to 31 October 1999**

To

Ronald D. Joslin  
National Aeronautics and Space Administration  
Langley Research Center  
1A East Reid St. Mail Stop 170  
Hampton, VA. 23681

By

William S. Saric  
Professor

Mechanical and Aerospace Engineering  
Arizona State University  
Box 87-6106  
Tempe, AZ. 85287-6106

October 1999

---

Janice D. Bennett, Director  
Office of Research Creative Activity  
(480) 965-8239

# Swept-Wing Receptivity Studies Using Distributed Roughness

William S. Saric

Mechanical and Aerospace Engineering

Arizona State University

Tempe, AZ. 85287-6106

## 1 INTRODUCTION

Transition to turbulence in swept-wing flows has resisted correlation with linear theory because of its sensitivity to freestream conditions and 3-D roughness and because one of the principal instability modes quickly becomes nonlinear. In the face of such a formidable problem, two rather long-term fundamental efforts have been underway at DLR Göttingen and Arizona State University that address swept-wing transition. These efforts have been recently reviewed by Bippes (1997) and Reibert and Saric (1997). Thus, the present work is a continuation of a series of studies on swept-wing boundary layers which have led to a better understanding of the transition process. In particular, we have taken advantage of the sensitivity to 3-D roughness and the modal nature of the instability in order to propose a particular control strategy.

Complementing the two aforementioned reviews, general reviews of the swept-wing transition problem are found in Arnal (1997) and Kachanov (1996). Other recent reviews include Reshotko (1997), Crouch (1997), and Herbert (1997a,b). The failure of linear theory is discussed in Reed et al. (1996). The historical work is found in Reed and Saric (1989).

The basic idea is that the combination of sweep and chordwise pressure gradient within the boundary layer creates a velocity component perpendicular to the inviscid streamline. This *crossflow* profile is inflectional and exhibits both traveling and stationary unstable waves called crossflow vortices that are (approximately) aligned along the inviscid streamlines. Under conditions of low freestream turbulence levels, the dominant crossflow wave is stationary (Reibert and Saric 1997) while moderate to high turbulence levels initiate dominant traveling waves (Dehle and Bippes 1996; Bippes 1997). The mechanism is relatively insensitive to sound and 2-D surface roughness (Radeztsky et al. 1993) but very sensitive to 3-D roughness near the attachment line.

We concentrate our work on low-turbulence freestream flows and stationary crossflow waves. Although the  $v'$  and  $w'$  components of the disturbances are very small, by convecting streamwise momentum in the wall-normal direction, they produce  $O(1)$  changes in  $u'$ . Thus the mean flow is highly distorted with localized inflection points. Transition is then triggered by a high-frequency secondary instability of the distorted mean profile (Kohama et al. 1991; Malik et al. 1994).

## 2 FACILITY AND MODEL

The ASU crossflow experiments are conducted in the Arizona State University Unsteady Wind Tunnel—a low-speed, low-turbulence, closed-circuit facility in which the stability and transition of laminar boundary layers are studied (Saric 1992a). The NLF (2)-0415 airfoil model (Somers and Horstmann 1985) is mounted vertically in the 1.4 m x 1.4 m x 4.9 m test section. Floor and ceiling contours installed in the test section produce an infinite-span swept-wing flow (Figure 1). With a 45° sweep and a -4° angle of attack, the favorable pressure gradient produces considerable crossflow while suppressing T-S modes (Figure 2). The efficacy of the wall liners in establishing spanwise uniform flow is shown in Figure 3 which is a superposition of 100 mean profiles of the streamwise component. The basic-state flow is found to be identical to Reibert et al. (1996).

The aluminum surface of the NLF (2)-0415 is hand polished to a 0.25  $\mu\text{m}$  rms finish in order to establish the smooth base state. Very small roughness elements, of minimum height of 6  $\mu\text{m}$  ( $Re_k \approx 0.1$ ), are introduced in a spanwise

periodic distribution<sup>1</sup>. These roughness elements linearly excite specific modes within the boundary layer at a level above the background level<sup>2</sup>. Detailed hot-wire measurements within the boundary layer provide two-dimensional maps of the stationary disturbance structure, while spectral techniques are used to identify and follow specific stationary modes. The details of the procedures have been established in Reibert et al. (1996), Reibert (1996), and Carrillo (1996).

### 3 NONLINEAR INTERACTION AND AMPLITUDE SATURATION

The work in this section re-establishes the basic ideas of nonlinear interaction along the lines of the results of Reibert et al. (1996). The basic ground rules are that we consider low-turbulence environments and stationary crossflow waves.

#### 3.1 Natural Roughness

In the absence of artificial surface roughness, the naturally occurring stationary crossflow waves are nonuniform in span due to submicron surface irregularities near the leading edge. This is shown in Figure 4, which displays a contour plot of the normalized boundary-layer velocity at  $x/c = 0.55$  for  $Re_c = 2.4 \times 10^6$ . The Figure shows that the streamwise velocity  $u/U_e$  in the  $(Y, z)$  plane. The flow is toward the reader (i.e., the observer is looking upstream into the oncoming boundary-layer flow), and the stationary vortices are turning in the right-handed sense. The velocity contours are constructed from 100 mean-flow boundary-layer profiles each separated by 1 mm in span. It is important to note that the wave-like structure of Figure 4 represents the integrated effect of the weak stationary vortices on the streamwise velocity.

Figure 4 displays a dominant feature at a 12 mm spanwise spacing, which is approximately the most amplified stationary wavelength according to linear theory. At the same time, the richness in the spectral content is evident and indicates nonlinear interaction among many modes. The random nature of the leading-edge roughness leads to the lulls found in the data of Figure 4. These data are typical of all the experiments in the early 1990's.

The difficulty with these data is that a computational model will decompose the unstable motion in modes and thus needs the individual mode behavior from the experiment if a meaningful comparison can be made. This information was not forthcoming in the earlier experimental work and Radeztsky et al. 1994 and Reibert et al. 1996 corrected the situation by considering a forced response of the boundary layer rather than rely on random disturbances.

#### 3.2 Critical Forcing

##### 3.2.1 Details of the Roughness Elements

The initial conditions are controlled by applying a full-span array of  $k = 6 \mu\text{m}$  roughness elements at  $x/c = 0.023$ . Whereas the height and spanwise spacing may vary, the roughness elements are always placed at the same chord location. At  $x/c = 0.023$ , the boundary-layer displacement thickness is approximately  $250 \mu\text{m}$  and  $Re_k \approx 0.1$  for  $k = 6 \mu\text{m}$ . Thus we expect a weak linear input to the unstable waves. The roughness elements are circular and the diameter is 3 mm except in the case of 8 mm spacing in which case the diameter is 2 mm. Radeztsky et al. (1993) provide data on the effect of chord location and diameter of the roughness.

##### 3.2.2 Excitation of the Critical Mode

The spanwise spacing of the elements is 12 mm, corresponding to the naturally occurring most-amplified wavelength. Figure 5 shows the streamwise velocity contour with the roughness installed. The dominance of the 12 mm mode is striking, and allows a direct calculation of the stationary disturbance amplitude (see Reibert et al. 1996 for a description of the technique).

Figure 6 compares the experimental amplification factor ("N-factor") for the 12 mm roughness forcing with the predictions of the Orr-Sommerfeld equation (OSE), the linear parabolized stability equations, and the full nonlinear

<sup>1</sup> A carefully painted surface has roughness on the order of  $6 \mu\text{m}$ .

<sup>2</sup> This is similar to the classic vibrating ribbon and T-S wave experiment except in this case the waves are stationary.

parabolized stability equations. All computational results are provided by Haynes (1996). The saturation phenomenon is clearly evident, and can be quantified. The early growth shows excellent agreement with linear PSE, however strong nonlinear effects develop well before transition at  $(x/c)_{tr} = 0.52$ . The importance of nonparallel effects is indicated by the failure of traditional linear stability theory (OSE) to accurately predict the growth even in the linear range. When nonlinearity is added, the agreement is remarkable over the entire measurement region and all aspects of the growth are predicted. This is explained in more detail in Reibert et al. (1996), Reibert (1996), Haynes and Reed (1996), and Haynes (1996).

The outstanding agreement shown in Figure 6 results from the inclusion of curvature in the computations, without which the disturbance growth is significantly overpredicted. The sensitivity to very weak curvature is due to the strong stabilizing Görtler effect with convex curvature (Benmalek and Saric 1994). This is the reason for the disagreement between the linear experiments of Radeztsky et al. (1994) and linear theory without curvature. More information on the sensitivity to curvature can be found in Haynes (1996).

### 3.3 Multiple-Mode Crossflow Waves

Reibert et al. (1996) produced multiple-mode crossflow waves by increasing the space between the roughness elements. Their streamwise velocity contours obtained with a roughness spacing of 36 mm showed a primary structure at 36 mm corresponding to the roughness spacing. In addition, higher wavenumber (shorter wavelength) modulations appeared due to superharmonics that are present at integer multiples of the primary wavenumber. This is clearly indicated by the power spectral density (PSD) calculations of Reibert et al. (1996) which showed amplified modes with wavelengths of 36 mm, 18 mm, 12 mm, 9 mm, 7.2 mm, 6 mm, 5.1 mm, 4.5 mm, and 4 mm. The presence of the roughness-induced harmonic sequence indicates that the stationary crossflow pattern is not predetermined by external flow conditions, but can be completely controlled by the surface characteristics.

## 4 ROLE OF SPANWISE SPACING

Two important observations concerning the data of Reibert et al. (1996) are:

1. Unstable waves occur only at integer multiples of the primary disturbance wavenumber, and
2. No subharmonic disturbances are destabilized.

In other words, spacing the roughness elements 12 mm apart excites disturbances with spanwise wavelengths of 6 mm and 4 mm. Spacing the roughness elements 36 mm apart excites disturbances with spanwise wavelengths of 36 mm, 18 mm, 12 mm, 9 mm, 7.1 mm, 6 mm etc. These spacing do not produce any unstable waves with “intermediate” wavelengths or with wavelengths greater than the imposed spacing.

Following this lead, we investigate the effects of distributed roughness whose primary disturbance wavenumber does not contain a harmonic at  $\lambda_x = 12$  mm (the most unstable wavelength according to linear theory).

### 4.1 Overview

All stationary crossflow amplitude data are acquired using the two hot-wire techniques explained in Reibert et al. (1996). Table 1 summarizes the five data sets examined in this study. The chord Reynolds number is shown in the column labeled  $Re_c$  and is fixed at  $2.4 \times 10^6$  for all cases. Columns  $k$  and  $\lambda_z$  show the roughness height and spanwise spacing, respectively, and the last two columns give the type of scan used. A bullet (•) in the BL and Span columns indicates wall-normal boundary-layer scans and constant-Y spanwise scans, respectively. Note that both scan types are used for all data sets.

Data Set	$Re_c/10^6$	Roughness		Scan Type	
		$k$ [ $\mu\text{m}$ ]	$\lambda_z$ [mm]	BL	Span
A	2.4	0	0	•	•
B	2.4	6	18	•	•
C	2.4	12	18	•	•
D	2.4	18	18	•	•
E	2.4	6	8	•	•

Table 1: Experimental data sets

To maintain consistency with Reibert (1996), the shorthand notation  $[k|\lambda_z]$  will be used to unambiguously define the roughness configuration. As outlined in Section 3.2.1, the roughness elements are applied in a full-span array at  $x/c = 0.023$  for all cases. Therefore specifying the roughness height and spacing fully determines the roughness configuration. Thus,  $[6|18]$  represents a full-span roughness array with a  $k = 6 \mu\text{m}$  element height and a  $\lambda_z = 18 \text{ mm}$  spanwise spacing. The natural roughness case, data set A, is given the notation  $[0|0]$ .

When presenting the results for individual-mode disturbance amplitudes, crossflow modes will be designated in the shorthand notation  $(f,m)$ , where  $f$  is the disturbance frequency and  $m$  is the mode number. The mode number is defined as the disturbance wavenumber normalized by the wavenumber of the fundamental mode. Thus,  $m = 1$  and  $m = 2$  indicate the fundamental disturbance and first superharmonic, respectively. The spanwise-invariant disturbance, typically called the “mean-flow distortion” mode, is presented by  $(0,0)$ .

#### 4.2 Natural Roughness—Data Set A

Some of these data have been presented in Figures 3 and 4 while the remainder are referenced to Carrillo (1996). Extensive measurements were carried out in this case to archive the natural roughness base state should anyone wish to tackle a computation of these results. The information on flow visualization and transition location will be discussed in a later section.

#### 4.3 $[6|18]$ Roughness—Data Set B

To generate stationary crossflow waves that are uniform in span and contain a fixed spectral content, artificial surface roughness elements are applied to the airfoil surface as explained in Section 3.2.1. These roughness elements provide fixed initial conditions for the stationary vortices. A full-span array of  $6 \mu\text{m}$  high roughness elements spaced  $18 \text{ mm}$  apart is applied at  $x/c = 0.023$ . Radeztsky et al. (1993a) shows that this chord location maximizes the effects of the applied roughness.

The  $18 \text{ mm}$  spacing was chosen to confirm that neither the  $12 \text{ mm}$  mode nor the  $36 \text{ mm}$  mode will be excited according to the observations described at the beginning of Section 4.

##### 4.3.1 Total Disturbance Amplitude

Figure 7 shows the normalized velocity contours at  $Re_c = 2.4 \times 10^6$  at  $x/c = 0.40$ . The  $18 \text{ mm}$  spacing is observed with a very strong  $9 \text{ mm}$  modulation. Even at  $x/c = 0.45$ , the small artificial roughness yields boundary-layer distortions that are very uniform and periodic in span.

The boundary-layer profiles from which the contour map of Figure 7 is made are shown in Figure 8. The mean profile is also shown and as with the no roughness case, the stationary disturbance has dramatically distorted the mean boundary layer. The spanwise-average profile is doubly inflected even for  $x/c \geq 0.30$ .

Figure 9 presents the total disturbance mode-shape profiles for  $0.10 \leq x/c \leq 0.45$ . Following Reibert et al. (1996), departure from the linear mode shapes begin to occur around  $x/c = 0.3$ . The growth of the disturbance is easily

characterized by the log of the amplitude ratio such as  $N = \ln(A/A_0)$ . Where  $A_0$  is the initial amplitude and  $N$  is commonly called the  $N$ -factor. The *measure* of the disturbance can be the (1) the maximum of the rms mode shape; (2) the integral of the rms in the wall-normal direction; (3) the integral of the square of the rms. Reibert et al. (1996) show that when cast in terms of the  $N$ -factor, the growth behavior is the same. Thus the max amplitude of the mode shapes of Figure 9 are used as a measure of growth. The top curve of Figure 10 is the growth of total signal. This curve shows dramatic amplitude saturation for  $x/c \geq 0.25$ . At these chord locations, the characteristic second lobe appears in the mode-shape profiles, indicating strong nonlinear effects.

#### 4.3.2 Individual-Mode Amplitude

A full set of spanwise scans are conducted to extract the modal content of the disturbance. The height scanned corresponds to the maximum of the total disturbance mode shape at each  $x/c$ . The power spectral density computations for these scans are computed. Integration of the peaks of these data are used to form Figure 10. Unstable modes are first detected at  $x/c = 0.10$ . The spectrum at this location shows energy in the (0,2) mode ( $\lambda_z = 9$  mm). Although there is a peak evident at  $\lambda_z = 18$  mm, its amplitude is very small and close to the noise of the spectrum. Based on a consistent definition of the spectral noise, the 18 mm peak is ignored. It is interesting that the (0,2) mode contains more energy than the fundamental ( $\lambda_z = 18$  mm).

The fundamental mode is not measurable until  $x/c = 0.20$ . Although the fundamental is detected, the first harmonic at  $\lambda_z = 9$  mm still contains most of the disturbance energy. The fundamental disturbance grows rapidly for  $0.35 \leq x/c \leq 0.45$ , where the (0,2) mode actually shows some decay. Higher harmonics become unstable for  $x/c \geq 0.25$ . The spectrum at  $x/c = 0.45$  shows detectable disturbances for the (0,3) and (0,4) modes ( $\lambda_z = 6$  mm and 4.5 mm). No amplified subharmonics (wavelength doubling) of the roughness spacing are detected. This is consistent with the finds of Reibert et al. (1996).

Note that the 12 mm wavelength, which is approximately the most unstable according to linear theory, is not amplified at any  $x/c$ . The 18 mm forcing has successfully suppressed the growth of this wavelength disturbance. Reibert et al. (1996) did not observe this because his roughness spacings were all multiples of 12 mm. Radeztsky et al. (1994) does show this phenomenon, however, his studies were at a different angle of attack ( $\alpha = 0^\circ$ ) with much larger roughness heights (146  $\mu\text{m}$ ).

In Figure 10 the (0,2) mode shows exponential growth up to  $x/c = 0.25$ , at which point the mode begins to saturate. The (0,2) mode reaches a maximum amplitude of 13% at  $x/c = 0.40$ , after which it decays. It is in this saturation and decay region ( $0.35 \leq x/c \leq 0.45$ ) of the (0,2) mode where the fundamental disturbance shows strong growth. This is also the region of strong nonlinear effects as seen by the growth of the second lobe in the total disturbance mode-shape profiles (Figure 9).

Also presented in Figure 10 are the corresponding  $N$ -factor distributions. Since the individual modes are first detected at different chord locations with different initial amplitudes, each wavelength  $N$ -factor curve is reference to a different amplitude. Thus, direct comparisons between the growth *rates*, however, are entirely meaningful. The amplitude of the (0,2) mode ( $\lambda_z = 9$  mm) agrees well with the total disturbance amplitude up to  $x/c = 0.30$ , the (0,2) mode amplitude drops from the total disturbance and the amplitudes of the fundamental and higher harmonics grow.

The most important feature of Figure 10, however, is that *the linearly most unstable disturbance* ( $\lambda_z = 12$  mm) *has been completely suppressed*.

#### 4.4 [12|18] and [18|18] Roughness—Data Sets C and D

Reibert (1996) observed the interesting feature that, for a fixed roughness spacing of  $\lambda_z = 12$  mm, the total disturbance amplitude grew to a constant saturation amplitude even when the roughness height was varied from 6  $\mu\text{m}$  to 48  $\mu\text{m}$ . Although the initial disturbance amplitude increased with larger roughness, the effects downstream relaxed and yielded similar looking mode shape. Data Sets C and D provide further evidence of this characteristic for the  $\lambda_z = 18$  mm roughness spacing.

The roughness height in this study is increased from 6  $\mu\text{m}$  to 12  $\mu\text{m}$  and then to 18  $\mu\text{m}$  by stacking the roughness elements. Transition occurs at  $x/c \approx 0.50$  for all three roughness heights. Since saturation amplitude comparisons are the primary concern, disturbance amplitude data are acquired only at  $x/c = 0.45$ . Both the total disturbance and individual-mode disturbance amplitudes are computed and compared. The details are given in Carrillo (1996).

Table 2 summarizes the amplitudes for the total and individual-mode disturbances at  $x/c = 0.45$ . As mentioned in the previous section, the total disturbance amplitude remains constant at about 14% with increasing roughness height. There does appear to be some redistribution of energy in the modal content as the initial conditions are increased. It is difficult, however, to make any meaningful conclusions about the effects of the larger roughness on the individual-mode amplitudes. As shown by the [6|18] roughness, forcing at  $\lambda_z = 18$  mm actually excites the 9 mm wavelength first, which grows rapidly, saturates, and then decays. It is possible that the larger roughness heights yield larger initial amplitudes for the 9 mm component, which would then grow, saturate, and decay sooner than for the [6|18] roughness case. This would explain the smaller (0,2) mode amplitudes, since the mode would be decaying over a larger distance by the time  $x/c = 0.45$  is reached. Of course this is all just speculation, and further study must be done before any definite conclusions can be made.

Roughness Height	Disturbance Mode Amplitude [%]				
	Total	$\lambda_z = 18$ mm	$\lambda_z = 9$ mm	$\lambda_z = 6$ mm	$\lambda_z = 4.5$ mm
6 $\mu\text{m}$	14.2	10.1	10.0	3.3	0.9
12 $\mu\text{m}$	14.8	12.8	8.3	2.7	0.5
18 $\mu\text{m}$	13.3	11.2	8.0	0.8	0.9

Table 2. Total and individual-mode amplitudes for  $Re_c = 2.4 \times 10^6$  and [k|18] roughness at  $x/c = 0.45$ .

#### 4.5 [6|8] Roughness—Data Set E

Section 4.4 shows the effective suppression of the most unstable wavelength by using a roughness spacing that does not contain superharmonics with wavelengths around 12 mm. In addition, no evidence of subharmonics in this and past experiments by Radeztsky et al. (1994) or Reibert et al. (1996) has ever been observed. Linear stability theory predicts that short wavelength disturbances grow early, saturate, and then decay. Thus, the next logical step is to study the effects of a subcritical roughness spacing ( $\lambda_z < 12$  mm).

Both linear stability theory and the 18 mm-spaced roughness experiments presented above show that the 9 mm wavelength is also very unstable. Therefore, it is desirable to space the roughness elements less than 9 mm apart. For this study, the 6  $\mu\text{m}$ -high roughness elements are applied in a full-span array at  $x/c = 0.023$  with a spanwise spacing of 8 mm.

##### 4.5.1 Flow Visualization

As for the [0|0] roughness case, surface-shear-stress patterns and transition locations are determined using naphthalene flow visualization. Figures 11 and 12 show the naphthalene pattern for the [0|0] and [6|8] cases, respectively at  $Re_c = 2.4 \times 10^6$ . Again, the flow is from left to right, and the leading edge and chord locations are marked<sup>3</sup>. The stationary crossflow vortices transpose high-and low-momentum fluid within the boundary layer, yielding a spanwise modulation of the surface shear stress. This modulation is clearly indicated as alternating streaks in the naphthalene. Regions in which the boundary layer is turbulent are indicated by complete sublimation of the naphthalene (dark area). Note that this does not hold true in the region near the leading edge, where naphthalene is not sprayed to prevent roughness contamination. Transition appears as a series of turbulent wedges, which is

<sup>3</sup> The white numerals represent the chord location in percent.

characteristic for swept-wing flows. Note that the transition pattern is nonuniform under natural surface roughness conditions. This is consistent with past experiments and is indicative of submicron roughness irregularities near the leading edge.

The transition pattern of Figure 12 is extremely interesting. The [6|8] roughness has effectively delayed transition *past* the pressure minimum location ( $x/c = 0.71$ ). In fact, transition has been moved back even past the transition location observed under natural surface roughness conditions (Figure 11). Transition occurs for the [6|8] roughness case at approximately 80% chord, which is the location of the junction between the wing and trailing-edge flap. Thus, it is entirely possible that the junction actually causes transition.

Figure 12 shows definite vortex streaks with an 8 mm spacing for  $0.30 \leq x/c \leq 0.45$ . For  $x/c > 0.45$ , however, the 8 mm structure “washes out” and the vortex streaks appear at larger spanwise spacings. Although the spacing between streaks becomes larger in general, there is definite spanwise nonuniformity in the spacing. Thus, it is difficult to make any conclusions about the longer wavelengths based solely on the flow visualization. Detailed boundary-layer measurements shed more light on the phenomenon.

For  $Re_c = 2.6 \times 10^6$  and [6|8] roughness, transition occurs at approximately 59% chord, which is comparable to the transition location for the no roughness case. Vortex streaks spaced at 8 mm are apparent up to about  $x/c = 0.45$ , at which point the longer wavelength structure appears. Transition again occurs in the this region where the longer spanwise spacing dominates.

The transition pattern for [6|8] roughness and  $Re_c = 2.8 \times 10^6$  moves forward to about 50% chord, which is slightly more forward than the location for the corresponding natural roughness case. As with the  $Re_c = 2.4 \times 10^6$  and  $2.6 \times 10^6$  cases, 8 mm-spaced vortex streaks are observed. For  $Re_c = 2.8 \times 10^6$ , however, the 8 mm structure extends to  $x/c = 0.50$ . Transition occurs in this region where the 8 mm structure dominates, and there is no evidence of the longer-wavelength vortex streaks.

In general, the [6|8] roughness shows the ability of subcritical roughness spacing to delay transition. For  $Re_c \leq 2.6 \times 10^6$ , the transition location is at least as far back as that induced even by the finely-polished natural surface roughness conditions

#### 4.5.2 Total Disturbance Amplitude

The normalized velocity contours for  $Re_c = 2.4 \times 10^6$  and [6|8] roughness are shown in Figures 13, 14 for chord locations  $x/c = 0.30$  and  $0.60$ , respectively. The disturbance is first measurable at  $x/c = 0.10$ , and a very uniform and dominant  $\lambda_z = 8$  mm mode develops for  $0.10 \leq x/c \leq 0.25$ . At  $x/c = 0.30$  (Figure 13), although the contour plot still shows a dominant 8 mm mode, there is noticeable development of some slight nonuniformity. This nonuniformity becomes more dramatic with increasing  $x/c$ , and the 8 mm structure fades out in favor of some longer wavelength disturbances. By  $x/c = 0.50$ , the dominance of the fundamental mode ( $\lambda_z = 8$  mm) is gone, and  $x/c = 0.60$  (Figure 14) the fundamental mode is indistinguishable in the velocity contours. This is consistent with the results of the naphthalene flow visualization discussed earlier.

The total disturbance amplitude  $N$ -factors computed from the mode shapes are presented in Figure 15. The total disturbance grows rapidly from  $0.10 \leq x/c \leq 0.30$ , at which point the amplitude saturates and then slows strong decay. At  $x/c = 0.30$ , the second lobe high in the mode shape is evident, indicating strong nonlinear effects. The amplitude continues to decay for  $0.30 \leq x/c \leq 0.45$ . At  $x/c = 0.45$ , the amplitude levels off and then shows a second region of strong growth for  $0.50 \leq x/c \leq 0.60$ . Reibert (1996) observed a similar two-stage growth in some of his data, but never experienced such a dramatic amplitude decay before the second growth region. The computation of the Nonlinear PSE by Haynes (1996) confirms the theory and experiment for the 8 mm excitation. For the nonlinear computations, the necessary initial conditions are determined by matching the total disturbance amplitudes of the computation and experiment at  $x/c = 0.10$ , where the disturbance is first measurable experimentally. The nonlinear PSE slightly underpredicts the initial strong growth, but it accurately predicts the maximum  $N$  reached by the first growth stage and even captures the dramatic amplitude decay. This indicates that the drastic decay is a nonlinear effect, since the linear computations do not predict this feature. The nonlinear PSE does not predict the second



growth stage downstream. This is expected because the second growth region is due to longer-wavelength broadband disturbances, and not the fundamental 8 mm or superharmonic disturbances. The nonlinear PSE code initially puts energy into the fundamental wavelength and then superharmonic modes are “turned on” as nonlinear effects cause them to grow above a specified threshold. Thus, as implemented here, the PSE will not be able to predict the longer wavelength modes downstream.

#### 4.5.3 Individual-Mode Amplitude

The modal content of the stationary vortex structure for [6|8] roughness is determined with spanwise scans and spectral analysis. Figure 16 shows the integration of the PSD peaks from constant-height spanwise scans for  $0.10 \leq x/c \leq 0.60$  and gives amplitude and N-Factor curves. The fundamental mode is first detected at  $x/c = 0.10$  and grows rapidly to  $x/c = 0.30$ . The (0,2) mode becomes measurable at  $x/c = 0.20$ . For  $x/c > 0.30$ , nonuniformities develop as longer wavelength modes grow and eventually become dominant. At  $x/c = 0.60$ , the spectrum shows no evidence of the fundamental and (0,2) modes, rather, the spectrum is dominated by broadband energy contained in longer wavelengths ( $\lambda_z \geq 10$  mm). This is similar to the [0|0] roughness results which show nonuniformities due to the excitation of longer wavelength disturbances. The details are given by Carrillo (1996). The fundamental mode shows excellent agreement with the total disturbance for  $0.10 \leq x/c \leq 0.25$ . For  $x/c \geq 0.30$ , the fundamental amplitude drops dramatically from the total disturbance amplitude. Unlike the results of [6|8] roughness and Reibert (1996), the total disturbance is *not* completely made up by the fundamental and its superharmonics. In other words, strong growth of the (0,2) mode is not seen in the region where the fundamental drops from the total disturbance ( $0.30 \leq x/c \leq 0.60$ ). Rather, the continuing growth of the total disturbance occurs because the longer wavelengths become unstable downstream. Note that the longer-wavelength disturbances are broadband and are not subharmonics of the fundamental disturbance.

In short,  $Re_c = 2.4 \times 10^6$  and [6|8] roughness delays transition past that of the natural roughness case. Strong early growth of the 8 mm mode effectively suppresses initial growth of the very unstable 9 mm and 12 mm modes near the leading edge, which linear stability theory predicts to be the region where these modes have the largest growth rates. The fundamental ( $\lambda_z = 8$  mm) mode saturates and then decays rapidly. This dramatic decay allows for longer wavelength background disturbances (due to submicron surface irregularities) to become unstable. The growth of these longer-wavelength broadband disturbances eventually leads to transition.

## 4 Conclusions

The most remarkable result obtained from the subcritical roughness spacing is the dramatic affect on transition location. In the absence of artificial roughness, transition occurs before the pressure minimum at  $x/c = 0.71$  for  $Re_c = 2.4 \times 10^6$ . Adding  $k = 6$   $\mu$ m roughness with a spanwise spacing equal to (or a multiple of) the wavelength of the linearly most unstable wave ( $\lambda_s = 12$  mm) moves transition forward to  $x/c \leq 0.52$ . However, the subcritical forcing at 8 mm spanwise spacing actually *delays transition beyond the pressure minimum and onto the trailing-edge flap at  $x/c = 0.80$* .

Boundary-layer transition in three-dimensional flows is a complicated process involving complex geometries, multiple instability mechanisms, and nonlinear interactions. Yet significant progress has been recently made toward understanding the stability and transition characteristics of swept-wing flows. It is worthwhile to repeat part of the summary of results from Reibert and Saric (1997). Concerning the crossflow problem, the past seven years have produced several important discoveries including:

- Development of instrumentation that can be applied to the flight-test environment.
- Application of POD methods to interpret wind-tunnel and flight-test transition data.
- Effect of environmental conditions in determining the relative importance of stationary and traveling waves.
- Existence of a secondary instability causing local transition in stationary-crossflow-dominated flows.
- Sensitivity of the stationary disturbance to leading-edge surface roughness.

- Importance of nonlinear effects and modal interaction.
- Development of nonlinear PSE codes to predict all aspects of stationary disturbance growth.
- Sensitivity of stationary wave growth to very weak convex curvature.
- Use of artificial roughness to control the disturbance wavenumber spectrum and delay transition.

Three-dimensional boundary-layer stability is still far from being completely explained. Important factors such as receptivity—the process by which external disturbances enter the boundary layer and create the initial conditions for an instability—are still not well understood. Yet in spite of these shortcomings, careful experiments and accurate computations have resulted in significant progress toward understanding a difficult problem.

## ACKNOWLEDGMENTS

This work was done with Mr. Ruben Carrillo and Dr. Mark Reibert who were graduate students at the time. The author thanks Dr. Keith Chapman and Dr. Tim Haynes who contributed to the measurements and computations. The technical support of Mr. Dan Clevenger is greatly appreciated.

## REFERENCES

- Arnal, D. 1997. Laminar-Turbulent Transition: Research and Applications in France. *AIAA Paper 97-1905*.
- Benmalek, A., Saric, W.S. 1994. Effects of curvature variations on the nonlinear evolution of Goertler vortices. *Phys. Fluids* 3(10):3353-3367.
- Bippes, H. 1997. Environmental conditions and transition prediction in 3-D Boundary layers. *AIAA Paper 97-1906*.
- Carrillo, R.B. Jr. 1996. *Distributed-Roughness Effects on Stability and Transition in Swept-Wing Boundary Layers*. Master's thesis, Arizona State University.
- Crouch, J. 1997. Transition Prediction and Control for Airplane Applications. *AIAA Paper 97-1907*.
- Dagenhart, J.R., Saric, W.S., Mousseux, M.C., Stack, J.P. 1989. Crossflow vortex instability and transition on a 45-degree swept wing. *AIAA Paper 89-1892*.
- Deyhle, H., Bippes, J. 1996. Disturbance growth in an unstable three-dimensional boundary layer and its dependence on environmental conditions. *J. Fluid Mech.* 316:73-113.
- Haynes, T.S. 1996. *Nonlinear Stability and Saturation of Crossflow Vortices in Swept-Wing Boundary Layer*. Ph.D. diss., Arizona State University.
- Haynes, T.S., Reed, H.L. 1996. Computations in nonlinear saturation of stationary crossflow vortices in a swept-wing boundary layer. *AIAA Paper 96-0182*.
- Herbert, T. 1994. Parabolized stability equations. In *Special Course on Progress in Transition Modelling*. AGARD R-793. Loughton, Essex: Specialized Printing Services Ltd. ISBN 92-835-0742-8.
- Herbert, T. 1997a. Transition Analysis of Flow over Aerodynamic Bodies. *AIAA Paper 97-1908*.
- Herbert, T. 1997b. On the Stability of 3-D Boundary Layers. *AIAA Paper 97-1961*.
- Kachanov, Y.S. 1996. Experimental studies of three-dimensional instability of boundary layer. *AIAA Paper 96-1976*.
- Kohama, Y., Saric, W.S., Hoos, J.A. 1991. A high-frequency secondary instability of crossflow vortices that leads to transition. In *Proc. R.A.S. Boundary Layer Transition and Control*, Cambridge, U.L.
- Malik, M.R., Li, F., Chang, C.L. 1994. Crossflow disturbances in three-dimensional boundary layers: Nonlinear development, wave interaction and secondary instability. *J. Fluid Mech.* 268:1-36.
- Radeztsky, R.H. Jr., Reibert, M.S., Saric, W.S., Takagi, S. 1993. Effect of micron-sized roughness on transition in swept-wing flows. *AIAA Paper 93-0076*.
- Radeztsky, R.H. Jr., Reibert, M.S., Saric, W. 1994. Development of stationary crossflow vortices on a swept wing. *AIAA Paper 94-2373*.

- Reed, H.L., Saric, W.S. 1989. Stability of three-dimensional boundary layers. *Ann. Rev. Fluid Mech.* 21:235-284.
- Reed, H.L., Saric, W.S., Arnal, D. 1996. Linear stability theory applied to boundary layers. *Ann. Rev. Fluid Mech.* 28:389-428.
- Reibert, M.S. 1996. *Nonlinear Stability, Saturation, and Transition in Crossflow-Dominated Boundary Layers*. Ph.D. diss., Arizona State University.
- Reibert, M.S., Saric, W.S., Carrillo, R.B. Jr., Chapman, K.L. 1996. Experiments in nonlinear saturation of stationary crossflow vortices in a swept-wing boundary layer. *AIAA Paper 96-0184*.
- Reibert, M.S., Saric, W.S. 1997. Review of Swept-Wing Transition. *AIAA Paper 97-1816*.
- Reshotko, E. 1997. Progress, Accomplishments and Issues in Transition Research. *AIAA Paper 97-1815*.
- Saric, W.S. 1992a. The ASU transition research facility. *AIAA Paper 92-3910*.
- Somers, D.M., Horstmann, K.H. 1985. Design of a medium-speed natural-laminar-flow airfoil for commuter aircraft applications. *DFVLR-IB/29-85/26*.

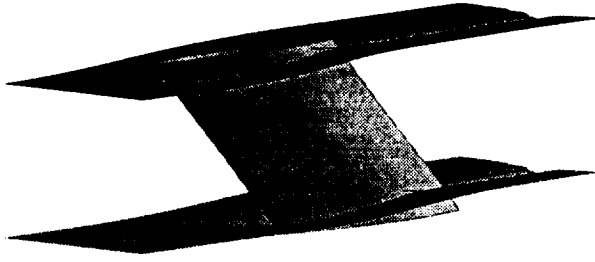


Figure 1. NLF(2)-0415 airfoil and wall liners.

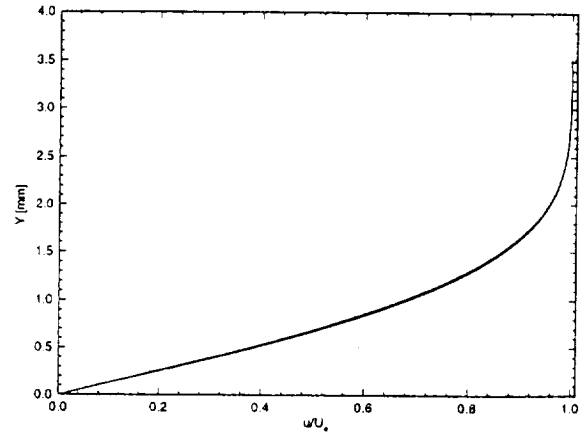


Figure 3. Basic-state boundary layer profiles at  $x/c = 0.20$ . Plot contains 100 superposed over 99 mm of span.

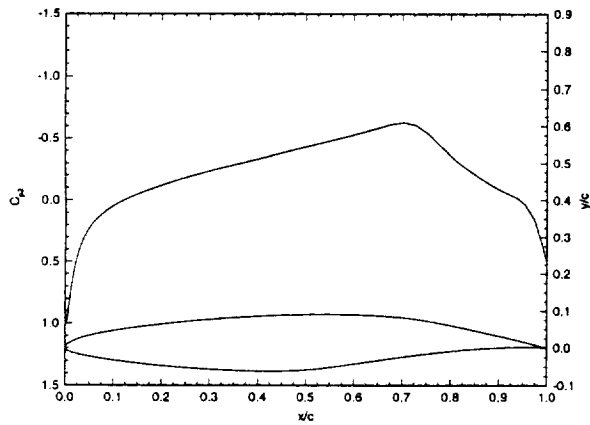


Figure 2. Unswept NLF(2)-0415 airfoil and upper surface  $C_p$  distribution for test conditions.

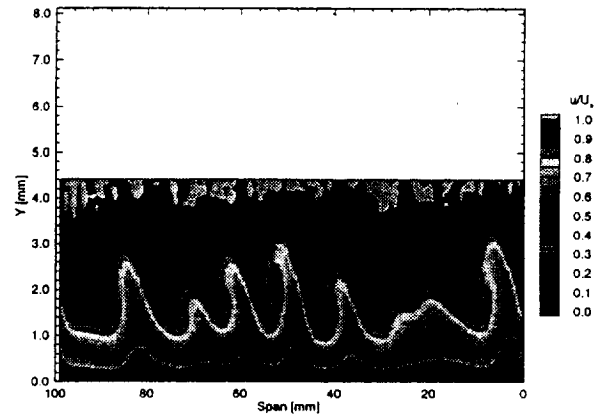


Figure 4. Streamwise velocity contours at  $x/c = 0.60$ .  $Re_c = 2.4 \times 10^6$ , no artificial roughness.

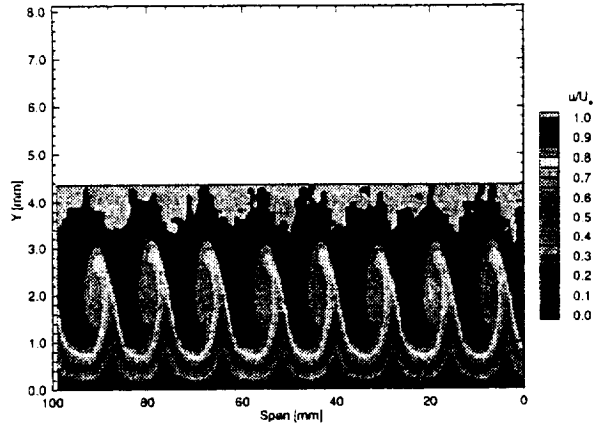


Figure 5. Streamwise velocity contours at  $x/c = 0.45$ .  $Re_c = 2.4 \times 10^6$ .  $k = 6 \mu\text{m}$  at 12 mm spacing.

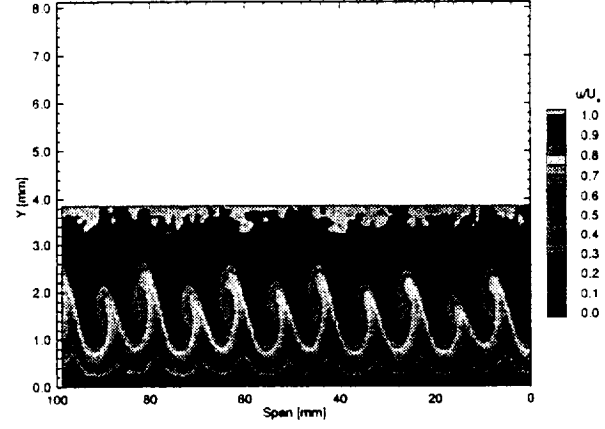


Figure 7. Streamwise velocity contours at  $x/c = 0.40$ .  $Re_c = 2.4 \times 10^6$ .  $k = 6 \mu\text{m}$  at 18 mm spacing.

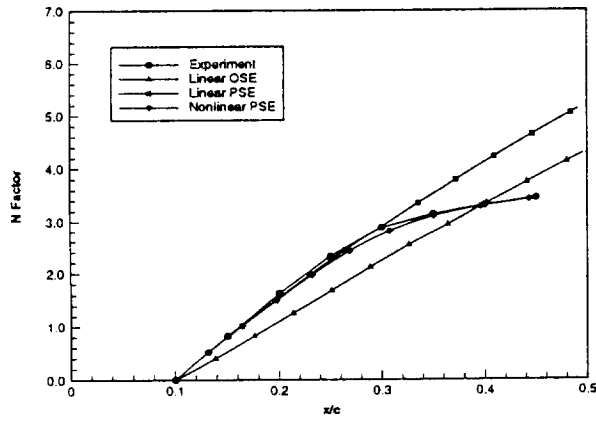


Figure 6. Measured and theoretical  $N$ -factors for the conditions of Figure 5. All theoretical calculations include curvature (Haynes and Reed 1996).

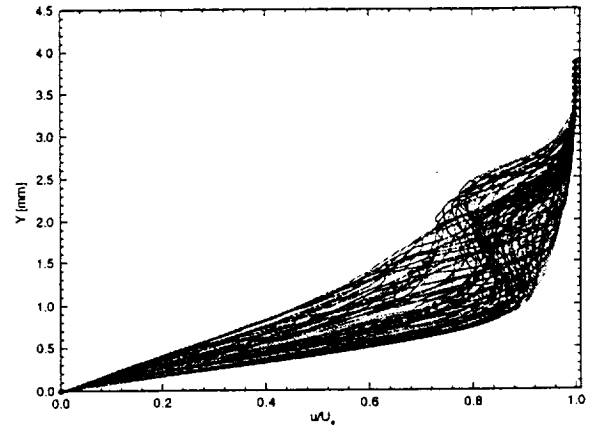


Figure 8. Spanwise array of 100 profiles spaced 1 mm apart at  $x/c = 0.40$ .  $Re_c = 2.4 \times 10^6$ .  $k = 6 \mu\text{m}$  at 18 mm spacing.

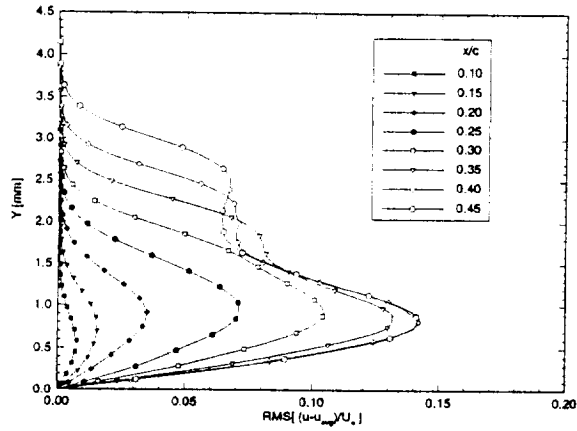


Figure 9. Stationary crossflow mode shapes. Conditions of Figure 8.

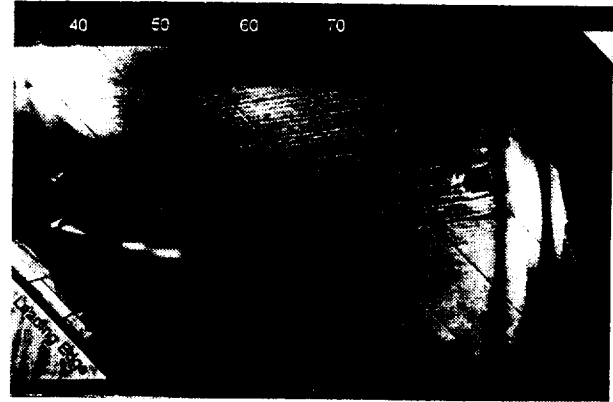


Figure 11. Flow visualization for  $Re_c = 2.4 \times 10^6$  and no artificial roughness.

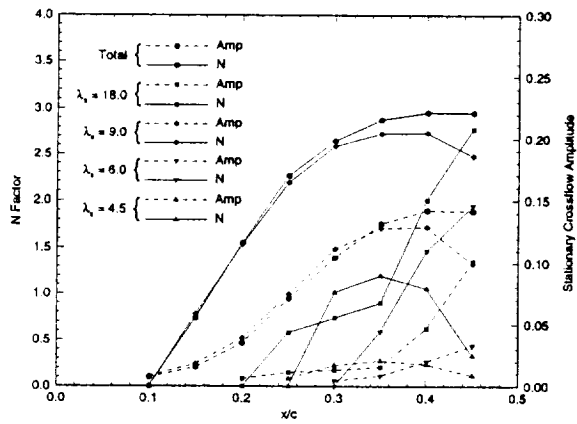


Figure 10. Total and single-mode disturbance amplitudes and N-factors. Conditions of Figure 8.

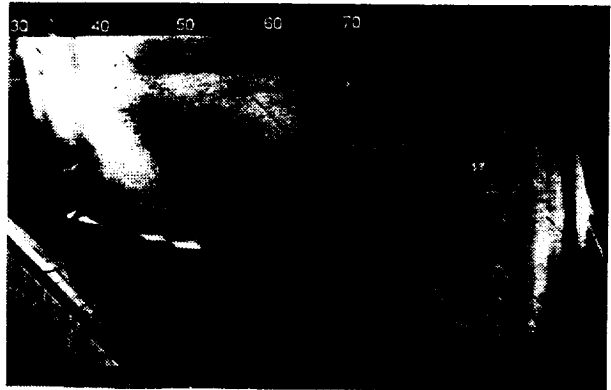


Figure 12. Flow visualization for  $Re_c = 2.4 \times 10^6$  with  $k=6 \mu\text{m}$  at 8 mm spacing.

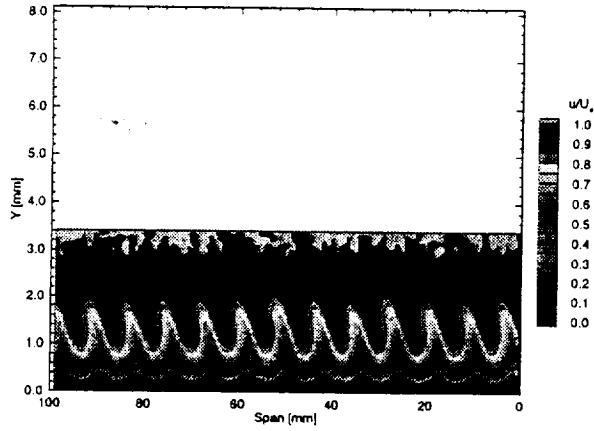


Figure 13. Streamwise velocity contours at  $x/c = 0.30$ .  $Re_c = 2.4 \times 10^6$ .  $k = 6 \mu\text{m}$  at 8 mm spacing.

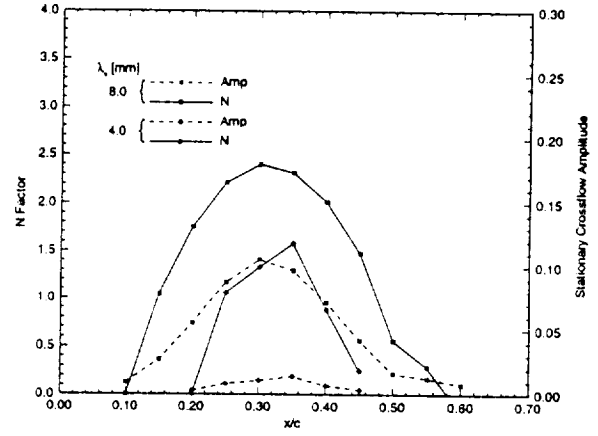


Figure 15. Total and single-mode disturbance amplitudes and  $N$ -factors. Conditions of Figure 13.

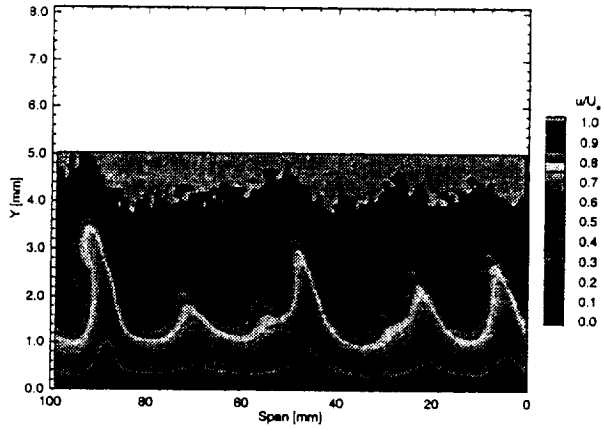


Figure 14. Streamwise velocity contours at  $x/c = 0.60$ . Conditions of Figure 13.